ORIGINAL PAPER

Influence of carbon structure/porosity on the electrochemical performance in Li–sulfur batteries

Barbora Pitňa Lásková[1] [ID] · **Markéta Zukalová**[1] · **Monika Vinarčíková**[1] · **Ladislav Kavan**[1]

Abstract

The porous structure of three different, commercially available porous carbonaceous materials is investigated by the α_S-plot method and by the *t*-plot method. Subsequently, the electrochemical properties of sulfur-free porous carbon electrodes from inspected materials are studied by cyclic voltammetry. The comparison of double-layer capacitances with the corresponding adsorption isotherms of N_2 reveals the role of micropores during the capacitive charging of carbons by Li^+. The studied carbons are added to the sulfur cathodes and evaluated. The cyclic voltammograms show no contribution of micropores in the carbon structure to the electrochemical processes taking place in the lithium–sulfur coin cell. The highest specific capacity of 816 mAh/g is observed for material with the lowest content of micropores in the structure (14%). The partially mesoporous and partially microporous (65%) sample and the predominantly microporous one (87%), show specific capacities of 664 mAh/g and 560 mAh/g, respectively. The galvanostatic cycling of lithium–sulfur coin cells with carbonaceous additives reveals that the mesopores and macropores in the carbon structure increase the specific charge capacity of the lithium–sulfur batteries and that the micropores improve the cycling stability of these batteries.

Graphical abstract
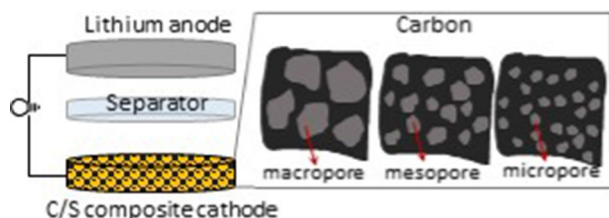
Introduction

The rising demand for energy storage devices with high energy density leads to intensive research on new battery systems. The lithium–sulfur (Li–S) battery is a promising system in this field, due to its non-toxicity, low cost, theoretical energy density of ca. 2600 Wh/kg, and capacity of 1675 mAh/g, which overcomes the commonly used lithium–ion batteries [1–3]. Sulfur is an abundant, inexpensive, and environmentally friendly element. Therefore, Li–S batteries have great potential for applications in such devices as drones [4, 5] and electric vehicles [6, 7]. Despite of undeniable promising properties of the Li–S system, some challenges have to be solved to enable the spreading of Li–S batteries into practical applications. The following limitations remain to impede the successful commercialization of Li–S cells. The Li metal usually serves as an anode that represents safety issues [8]. During the discharge process, the sulfur is reduced to lithium sulfide (Li_2S) at the cathode side. This process has multiple steps, in which sulfur is initially reduced to long-chain

✉ Barbora Pitňa Lásková
  barbora.laskova@jh-inst.cas.cz

1   J. Heyrovský Institute of Physical Chemistry, Czech
    Academy of Sciences, Dolejškova 3, 18223 Prague 8,
    Czech Republic

polysulfides (Li_2S_{6-8}), followed by a further reduction to form short-chain polysulfides (Li_2S_{2-4}) and final transformation to insoluble Li_2S. The sulfur reduction to Li_2S is connected with the volumetric expansion of the cathode and poor conductivity of both the reactant and the product [9]. Moreover, the intermediate lithium polysulfides are soluble and cause the well-known shuttle effect leading to a decline in cycle life and capacity [10]. In recent years, huge attention has been paid to all above-mentioned problematic aspects; however, some questions remain to be addressed.

Conductive carbons are widely used in various technologies and play a significant role in Li–S batteries. The above-mentioned problem of the electrically insulating nature of sulfur in the Li–S system is solved by embedding the active material into/on the conductive carbon. Various forms of carbon were widely used as cathode materials in Li–S batteries—spheres [11], nanofibers [12], nanotubes [13, 14], 3D [15, 16], and porous materials [17, 18]. Besides the improvement of cathode conductivity, the possibility of anchoring sulfur and the products of its reduction in carbon structure was studied [19, 20]. The characterization of the porous structure of carbon is crucial for a given application. According to the International Union of Pure and Applied Chemistry (IUPAC) definition, porous materials can be classified into three different categories based on pore size: microporous with pore widths smaller than 2 nm, mesoporous with pore widths 2–50 nm and macroporous with pore widths larger than 50 nm [21]. The micropores have two subgroups: ultramicropores (pore widths < 0.7 nm) and supermicropores (pore widths 0.7–2 nm). The commonly used method for pore structure characterization of carbonaceous materials is the physical adsorption of nitrogen and subsequent analysis of adsorption isotherms. Effective textural characterization of porous carbons is provided by comparative t-plot and α_S-plot methods [21–24]. Another useful technique is the subtracting pore effect (SPE) method applied to a high-resolution α_S-plot (based on isotherms from relative pressure 10^{-6}–1) [25–28].

The effect of different pores in the structure of carbon on the electrochemical performance of Li–S batteries has been widely discussed recently, but the role of carbon micropores in the cathode material is not yet fully clarified [2, 29–35]. Our current work aims at further elucidation of this issue. We report here a detailed study of the porous structure of three different, commercially available porous carbonaceous materials by subtracting pore effect method applied to a high-resolution α_S-plot and by the t-plot method. These three carbons are used as sulfur-free cathodes and as additives in the sulfur cathodes and their electrochemical behavior is studied to evaluate the effect of micro-/meso-/macropores of carbon material on the electrochemical performance of a corresponding cathode.

Results and discussion

Material characterization

The powder materials C_{Fluka}, C_{Penta}, and C_{TOB} (see "Experimental" for details) were characterized by Raman spectroscopy (Fig. 1). Two main Raman features of carbonaceous materials are observed in the spectra of all studied samples. The first one centered at ca. 1325 cm^{-1} belongs to the D-band, which is connected with the breathing mode and requires disorder or defect in the sp^2 carbon network for its activation [33, 36–40]. The D mode is dispersive, i.e. its frequency scales linearly with the photon excitation energy. The second band, the G-band at ~ 1590 cm^{-1}, arises from the symmetrical stretching mode of graphitic domains with sp^2 hybridization. The decoupled D to G peak intensity ratio (denoted as I_D/I_G) can be considered as a straightforward indicator of disorder in sp^2 systems, i.e. this ratio can point to differences in the graphitization degrees of carbon materials. The calculated intensity ratio I_D/I_G for the three studied carbonaceous materials are 1.23, 1.04, and 1.28 for C_{Fluka}, C_{Penta}, and C_{TOB}, respectively. The I_D/I_G ratios of C_{TOB} and C_{Fluka} are similar and indicate more disordered structures and a higher number of defects in these materials compared to C_{Penta}. The lower ratio for C_{Penta} shows a possibly higher degree of graphitization than for C_{TOB} and C_{Fluka}.

All carbon materials were investigated by nitrogen adsorption at 77 K for the relative pressures P/P_0 from 10^{-6} to 1. Figure 2 shows the adsorption isotherms of C_{Fluka}, C_{Penta}, and C_{TOB}. The studied powders have different porous structures. The adsorption isotherm of C_{Fluka} corresponds to type I according to the IUPAC classification with a sharp knee and high uptakes at relatively low pressures characteristic for microporous materials. The adsorption isotherm of C_{Penta} shows the features of type I and type
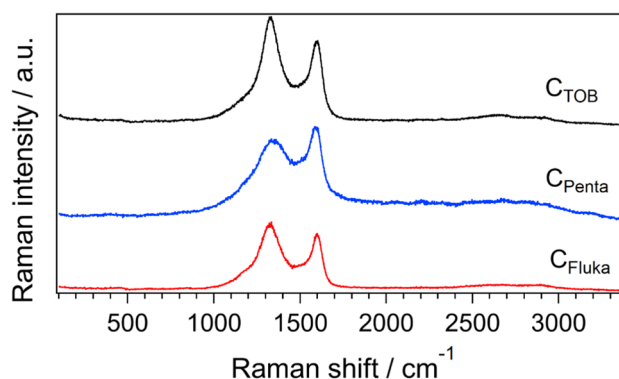

Fig. 1 Raman spectra of the pristine carbonaceous materials C_{TOB} (top, black), C_{Penta} (middle, blue), and C_{Fluka} (bottom, red) determined at an excitation wavelength of 633 nm. Spectra are offset for clarity but the intensity scale is identical (color version available online)
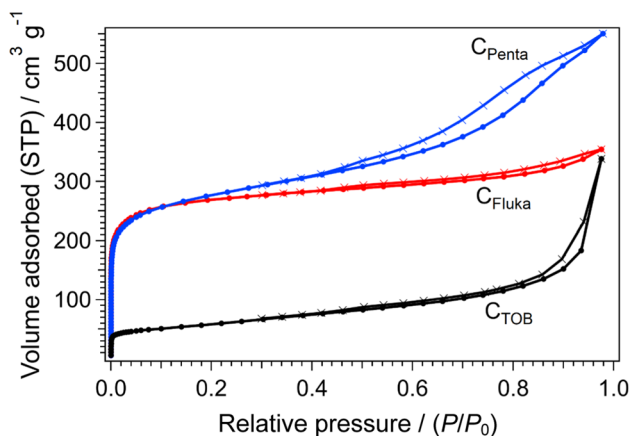
Fig. 2 Nitrogen adsorption isotherms at 77 K measured on carbonaceous materials (from top to bottom) C_{Penta}, C_{Fluka}, and C_{TOB}. The adsorption branch of the isotherm is marked by full circles and the desorption branch by crosses (color version available online)

IV isotherms. It exhibits significant nitrogen adsorption at low pressures indicating the presence of narrow micropores (pore width < 2 nm) and hysteresis loop at P/P_0 higher than 0.4 indicating the presence of mesopores in the structure. The C_{TOB} adsorption isotherm has a shape close to type II isotherm, which is normally associated with the external surface of non-porous material or with macroporous powders. The N_2 adsorption at low P/P_0 can indicate a minor contribution of micropores in structure. Table 1 shows the calculated BET specific surface areas for all our samples. The C_{Fluka} material has the highest specific surface area 1039 m^2/g. The C_{Penta} has a BET surface area comparable with C_{Fluka} (1028 m^2/g). On the other hand, the C_{TOB} sample has a five times lower specific surface area compared to the former.

Subsequently, the adsorption isotherms were analyzed by a comparative method of high-resolution α_S-plots. Wang et al. [25] tested six different non-graphitized carbon blacks as non-porous reference adsorbents for the α_S-plot analysis of porous carbons. Their carbon denoted as CB-1 (Monarch 280, Cabot Corporation) had the best properties for use as a standard in comparative α_S-plot analysis [25]. Therefore,

Table 1 Surface areas determined from BET, α_S-method and t-method using N_2 isotherms (S_{BET}—BET surface area, S_{tot}—total surface area from analysis of α_S-plot, S_{ext}—external surface area from analysis of α_S-plot and $S_{out\ of\ mic}$—surface area out of micropores from t-plot analysis)

Sample	$S_{BET}/m^2/g$	α_S-plot analysis		t-plot analysis
		$S_{tot}/m^2/g$	$S_{ext}/m^2/g$	$S_{out\ of\ mic}/m^2/g$
C_{Fluka}	1039	1127	25	140
C_{Penta}	1028	1085	31	358
C_{TOB}	205	206	193	177

the reference data from the N_2 (77.4 K) adsorption isotherms of Monarch 280 (Table S2 in Ref. [25]) were used as a standard α_S-curve for the construction of α_S-plots of our studied samples (C_{Fluka}, C_{Penta}, and C_{TOB}). The final high-resolution α_S-plots of C_{Fluka}, C_{Penta}, and C_{TOB} are shown in Fig. 3. The α_S-plots of C_{Fluka} and C_{Penta} have two upward swings for $\alpha_S < 1$ (below micropore saturation). These swings are a consequence of the adsorption in micropores. The first swing for $\alpha_S < 0.5$ ($P/P_0 < 0.007$) is called the *filling swing* and it is connected with monolayer adsorption in micropores enhanced by overlapping adsorption potentials of micropore walls [21, 25, 27]. The second upward swing at α_S between 0.5 and 1 is observed in the case the larger micropores (width > 1 nm [26]) are present in the carbon structure. This upward adsorption enhancement is the effect of continuous micropore filling in the remaining space of the micropore after the monolayer adsorption and it is called the *cooperative swing* [26, 27] or sometimes the *condensation swing* [28, 41]. There is a plateau of N_2 adsorption for C_{Fluka} in the region of micropores saturation ($\alpha_S > 1$) (see Fig. 3). On the other hand, the plateau for sample C_{Penta} is visible at higher α_S compared to C_{Fluka} and the plot corresponds to the C_{Penta} isotherm in Fig. 2 with obvious capillary condensation in mesopores. The α_S-plot observed for C_{TOB} material evidences a high rate of linearity (see Fig. 3). Generally, the linearity of the α_S-plot corresponds to unrestricted monolayer-multilayer adsorption typical for non-porous or macroporous solids [21]. Only the slight upward shifts for $\alpha_S < 0.5$ and $\alpha_S > 1$ indicate some content of micropores and mesopores, respectively, in the C_{TOB} structure. The material producer (TOB New Energy) declares the C_{TOB} to be a
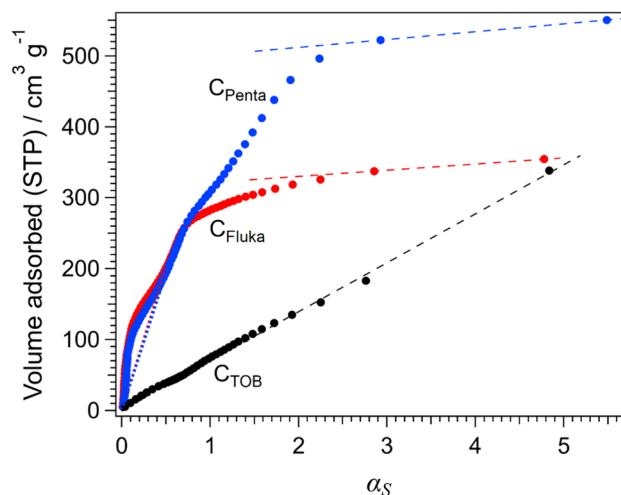

Fig. 3 The α_S-plots for C_{Penta} (top, blue), C_{Fluka} (middle, red), and C_{TOB} (bottom, black) materials. Dotted lines: the linear fits passing through the origin were used for total surface areas determination. Dashed lines: the linear fits for estimation of external surface areas (color version available online)

porous material with a pore diameter of about 130–150 nm (i.e. macropores), but their mercury intrusion porosimetry tests revealed intrusion peak in the range of pore sizes 20–200 nm. This agrees with our observed almost linear shape of the C_{TOB} α_S-plot (see Fig. 3). The SPE method was applied to high-resolution α_S-plots, and the total surface areas of studied powders were determined from the slope of the linear fit of α_S-plot passing through 0 and $\alpha_S \approx 0.5$. The difference between the BET surface area and the total surface area determined from the α_S-plot for the C_{TOB} sample is negligible. On the other hand, the α_S-plot total surface areas of C_{Fluka} and C_{Penta} are slightly higher (8% and 6%, respectively) compared to corresponding BET surface areas (see Table 1). The reason for this inconsistency is that the BET surface area of C_{Fluka} and C_{Penta}, even with the use of Rouquerol's criteria [42], is underestimated due to insufficient monolayer adsorption of nitrogen on micropores [25, 41]. Kaneko et al. introduced the external surface (surface out of micropores and mesopores) estimation from the almost plateau region of α_S-plot at high values of α_S [27]. This procedure was used for the determination of the external surface of our studied porous carbonaceous materials. Figure 3 shows the fits of respective α_S-plots. The fitted region for C_{TOB} was chosen across all the α_S values outside the micropore region, due to the high linearity of C_{TOB} α_S-plot, which is typical for non-porous/macroporous samples, where most of the surface area is external or in macropores. Table 1 summarizes the surface area analysis by α_S-plot method and the surface areas out of micropores ($S_{out\ of\ mic}$) determined by t-plot analysis. The data show the highest percentage of micropores ($S_{BET} - S_{out\ of\ mic}$; 87%) in the structure of the C_{Fluka} material. The C_{Penta} has an external surface area comparable with C_{Fluka} but the contribution of micropores to the overall surface area is lower (65%). On the other hand, the C_{TOB} sample has low amount of micropores in the structure (14%).

Electrochemical performance

Recently, the carbon pores and primarily micropores in the cathode material and their effect on the electrochemical performance of Li–S batteries have been widely discussed. There is still a lack of clarity on their role [2, 29–31, 33, 34] and the influence on capacity and stability [2, 29, 30, 32, 35]. Therefore, we focused on the electrochemical behavior of carbonaceous materials C_{Fluka}, C_{Penta}, and C_{TOB} in detail.

First, the electrochemical properties of sulfur-free porous carbon electrodes C_{Fluka}, C_{Penta}, and C_{TOB} were studied by cyclic voltammetry, where 40% of carbon C65 was added to electrodes for conductivity improvement (for details see "Experimental"). The cyclic voltammograms were carried out at scan rates 10, 5, 2, and 1 mV/s in potential window from 2 to 3 V vs Li/Li$^+$. Figure 4 shows cyclic
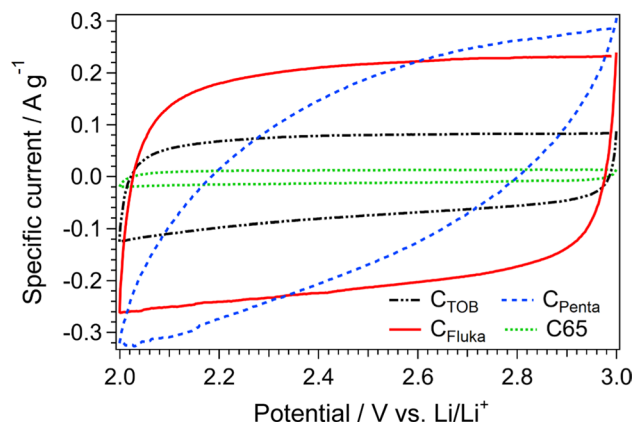

Fig. 4 Double layer capacitance measurement obtained by cyclic voltammetry at scan rate 5 mV/s. For line coding of cyclic voltammograms see the annotation in the chart (color version available online)

Table 2 Double layer capacitances normalized per gram of material (C_{DL}) from cyclic voltammetry of our sulfur-free cathodes at different scan rates (ν) by Eq. (1)

C_{DL}/F/g				
ν/mV/s	C_{TOB}	C_{Penta}	C_{Fluka}	C65
10	15.5	22.5	42.1	2.4
5	15.5	35.8	43.0	2.5
2	14.2	54.3	42.2	2.2
1	12.2	71.1	39.3	1.9

The current responses at the potential 2.5 V were considered for computations (the capacitance contribution of the C65 additive is not subtracted, because it was negligible and identical for C_{Fluka}, C_{Penta}, and C_{TOB} electrodes)

voltammograms of C_{Fluka}, C_{Penta}, C_{TOB} and pure C65 at a scan rate of 5 mV/s. The cyclic voltammograms of C_{Fluka} and C_{TOB} have an expected rectangular shape typical for capacitive charging. The C_{Penta} exhibited quasi-rectangular voltammograms for scan rates 2 mV/s and lower. The low contribution of C65 to the overall cyclic voltammetry response of C_{Fluka}, C_{Penta}, and C_{TOB} is evident from Fig. 4. The double layer capacitance (C_{DL}) was determined from cyclic voltammetry data according to Eq. (1):

$$C_{DL} = (I_a - I_c)/2\nu \tag{1}$$

where I_a (I_c) is the anodic (cathodic) current at a fixed potential and ν is the scan rate. Table 2 summarizes the double layer capacitances per gram of material calculated for each material and each scan rate from current responses at potential 2.5 V. The C_{Fluka} and C_{Penta} have at least two times higher C_{DL} compared to C_{TOB} for scan rates of 5 mV/s and slower. It agrees with the data of total surface areas S_{tot} in Table 1, where the C_{TOB} has the lowest total surface area (206 m^2/g)

and C_{Fluka} has the highest one (1127 m²/g), but close to S_{tot} of C_{Penta} (1085 m²/g). However, the S_{tot} of C_{Fluka} and C_{Penta} contains a high contribution of surface area in micropores (87% and 65%, respectively) compared to C_{TOB} (14%, see Table 1). Therefore, the data of C_{DL} in Table 2 indicate, that the micropores play a role in carbon capacitive charging by Li⁺. Almost negligible changes of C_{DL} for C_{TOB} and C_{Fluka} at different scan rates are evident from Table 2. These data indicate solely capacitive current's contribution to the overall current response of these carbonaceous materials. The C_{DL} increase is observed for slower scan rates of C_{Penta} carbon. This can be caused by the more complex porous structure of the material, which is the mixture of a high percentage of micropores and mesopores.

Second, the C_{Fluka}, C_{Penta}, and C_{TOB} were studied as additives in the sulfur composite cathode in the 2032-coin cells containing Li anode, and a glass microfiber separator. The coin cells were investigated by cyclic voltammetry and by galvanostatic chronopotentiometry. Cyclic voltammetry represents an analytic tool providing information about the charge capacity and the processes taking place during the electrochemical reaction. Figure 5 shows the cyclic voltammograms (2nd scan) of the C_{Fluka}, C_{Penta}, and C_{TOB} composite cathodes in a Li–sulfur cell measured at the scan rate of 0.1 mV/s. The cyclic voltammograms exhibit two reduction peaks at the potentials near 2.34 V and 2.02 V, and one oxidation peak at ca. 2.40 V. The first cathodic peak at 2.34 V is assigned to the reduction of S_8 to polysulfides Li_2S_x ($3 \leq x \leq 8$), and the second cathodic peak near 2.02 V is assigned to subsequent reductions up to Li_2S_2 and Li_2S. A single oxidation peak at 2.4 V for C_{Fluka} and C_{Penta} is observed due to the sluggish kinetics of the solid–liquid two-phase oxidation from the insoluble L_2S or Li_2S_2 to short-/long-cha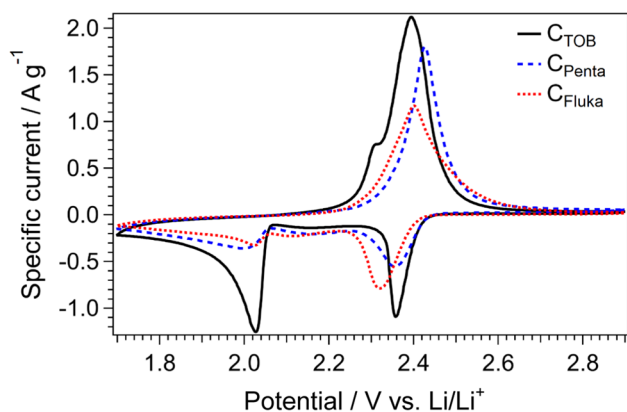in polysulfides, which causes an overlap of the corresponding peak in the oxidation branch of the cyclic voltammogram with that corresponding to oxidation of long-chain polysulfides to sulfur. The doublet of anodic peaks is distinguishable for C_{TOB} only. The specific charge capacities of C_{Fluka}, C_{Penta}, and C_{TOB} composite cathodes calculated from the oxidation (charge) branch of the cyclic voltammogram are 560 mAh/g, 664 mAh/g, and 816 mAh/g, respectively. The C_{TOB}, consisting mainly of wide pores, evinces the highest specific capacity. Conversely, both C_{Fluka} and C_{Penta} with high contribution of micropores in the structures have lower specific capacities than C_{TOB}. This trend is inverse as compared to the case of double-layer capacities from cyclic voltammograms of C_{Fluka}, C_{Penta}, and C_{TOB} in sulfur-free electrochemical cells discussed above (see Fig. 4 and Table 2).

The corresponding coin cells were subsequently studied by galvanostatic cycling. The electrochemical performance of the sulfur composite cathodes with C_{Fluka}, C_{Penta}, or C_{TOB} was studied by galvanostatic chronopotentiometry at the charging/discharging rate of 0.1 C. Figure 6 shows the galvanostatic curves of the C_{Fluka}, C_{Penta}, or C_{TOB} sulfur cathode during 60 charge/discharge cycles. The C_{TOB} sulfur cathode exhibits the largest capacities but also the largest decrease in capacity during 60 cycles. The partially mesoporous and partially microporous C_{Penta} (see Table 1) exhibits lower capacities than C_{TOB} and good stability over 60 cycles. There is an evident trend of specific charge capacity increase with an increasing percentage of mesopores/macropores in the carbon structure in Fig. 6, which is caused by the conservation of polysulfides in the meso/macropores during the charging/discharging process and suppressing their shuttle effect. On the contrary,
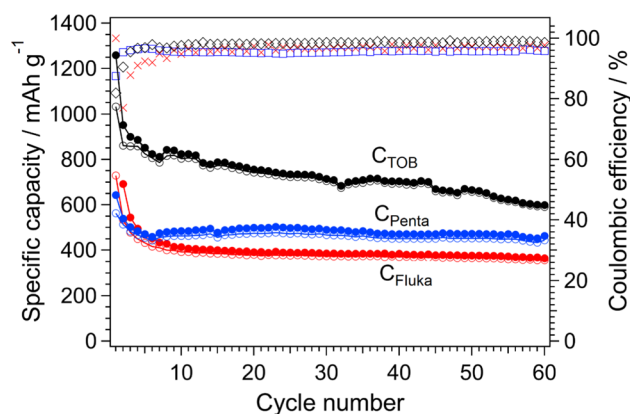

Fig. 5 Cyclic voltammograms (2nd scans) measured on the coin cell with sulfur composite cathode with C_{Fluka} (dotted line, red), C_{Penta} (dashed line, blue), and C_{TOB} (full line, black). Scan rate 0.1 mV/s. Currents are normalized to the mass of sulfur (color version available online)

Fig. 6 Galvanostatic chronopotentiometry curves measured at 0.1 C of Li–S cells containing sulfur composite cathodes with C_{TOB} (top, black circles), C_{Penta} (middle, blue circles), and C_{Fluka} (bottom, red circles). Charging curves are denoted by full circles, and discharging curves by open circles. The coulombic efficiencies are depicted by empty diamonds (C_{TOB}, black), empty squares (C_{Penta}, blue), and crosses (C_{Fluka}, red) (color version available online)

the cathode with microporous C_{Fluka} exhibited the lowest capacities after the first 10 cycles, but stable electrochemical performance during further cycling. Interestingly, the C_{Fluka} and C_{TOB} with similar content of defects in the structure (see Fig. 1) have very different trends in stability during cycling. Electrochemical data indicate that carbonaceous additives with wider pores (mesopores/macropores) and a more opened surface provide higher specific charge capacities in a sulfur composite cathode than microporous ones. Hence, mesoporous/microporous carbons represent the optimum additive for sulfur composite cathode in Li–S batteries. However, the more complex structure of C_{TOB} exhibiting wide pore size distribution (including 14% of micropores) manifests itself by structural instability during 60 days charging/discharging due to its inability to buffer the volume changes during the formation of soluble polysulfides (discharging) and backward deposition of sulfur (charging). The structural changes result in a pronounced capacity drop during cycling. On the other side, the structure of microporous C_{Fluka} is stable during 60 cycles, but exhibits lower specific capacity despite its high specific surface area. The observed low capacity and the fact that most of the specific surface area of C_{Fluka} is located inside the micropores (see Table 1) prove the low participation of micropores in the electrochemical reduction of sulfur and polysulfides oxidation, which is opposite to sulfur-free electrochemical cells discussed above (see Fig. 4 and Table 2). This conclusion agrees with the observed cyclic voltammogram of C_{Fluka} in Fig. 5. The low size of micropores (pore widths < 2 nm) represents a spatial constraint on sulfur accommodation. Li et al. observed the current peak with a maximum at 1.7 V for specially prepared sulfur-microporous carbon composite material and this peak was assigned to the solid–solid process, the reduction of smaller sulfur molecules confined within the micropores [43]. However, there is no additional current increase observed at potentials near 1.7 V for the cyclic voltammogram of C_{Fluka} in Fig. 5. This can also explain the good stability of C_{Fluka} and C_{Penta} during cycling. The sulfur composite cathode employing materials with a high percentage of micropores in the structure (C_{Fluka}/C_{Penta}) does not stress the micropores during charging/discharging by volumetric changes. This represents a significant stabilization factor. Indeed, the C_{Penta} exhibits nearly no capacity decay over 60 cycles in contrast to C_{TOB}. The majority of its surface area in micropores seems to compensate for the effect of disintegration during cycling. In summary, mesopores and particularly macropores in the carbon structure increase the specific charge capacity of the cathodes in the coin cell due to a spatial constraint of polysulfides near the sulfur composite cathode. On the other hand, micropores suppress carbon structure disintegration during cycling and thus improve the stability of the sulfur composite cathode.

Conclusion

Three commercially available porous carbon materials (C_{Fluka}, C_{Penta}, and C_{TOB}) were studied in detail by subtracting pore effect method applied to a high-resolution α_{S}-plot and by t-plot method to characterize their porous structures. The C_{Fluka} has the highest specific surface area 1039 m^2/g and is found to be a primarily microporous material with the highest ratio of micropores (87%) in the structure as compared to C_{Penta} and C_{TOB}. The C_{Penta} is a mesoporous/microporous material with a specific surface area comparable with C_{Fluka} (1028 m^2/g). The contribution of micropores to the overall surface area is lower (65%). On the other hand, the C_{TOB} sample contains a minority of micropores in the structure (14%) and exhibited N$_2$ adsorption isotherm typical for non-porous or macroporous materials. Raman spectroscopy proved highly defective structures of all carbonaceous samples.

The electrochemical behavior of carbonaceous materials C_{Fluka}, C_{Penta}, and C_{TOB} was studied in detail to evaluate the effect of micro-/meso-/macroporosity of the carbonaceous material on the electrochemical performance of corresponding cathodes. The electrochemical properties of sulfur-free porous carbon electrodes C_{Fluka}, C_{Penta}, and C_{TOB} were studied by cyclic voltammetry. The double-layer capacities of C_{TOB} and C_{Fluka} for different scan rates indicate solely capacitive charging of these carbonaceous materials. The C_{DL} increase was observed for slower scan rates of C_{Penta} carbon, which can be caused by the more complex porous structure of the material, which is the mixture of a high percentage of micropores and mesopores. Moreover, the comparison of C_{DL} data with corresponding total surface areas of C_{Fluka}, C_{Penta}, and C_{TOB} reveals the appreciable role of micropores during capacitive charging of carbons by Li$^+$. To study the effect of carbonaceous additives on the electrochemical performance of a corresponding sulfur composite cathode, the C_{Fluka}, C_{Penta}, and C_{TOB} were added to the sulfur cathodes and evaluated by cyclic voltammetry and galvanostatic chronopotentiometry. The cyclic voltammograms reveal a standard electrochemical behavior of these cathodes with no contribution of micropores in electrochemical processes. The highest specific capacity of 816 mAh/g is observed for C_{TOB}. The partially mesoporous C_{Penta} shows a specific capacity of 664 mAh/g and the microporous C_{Fluka} 560 mAh/g. The cycling by galvanostatic chronopotentiometry reveals excellent stability for both micropores-containing materials: C_{Fluka} and C_{Penta}. The mesopores and mainly macropores in the carbon structure increase the specific charge capacity of the Li–S batteries based on electrolyte 1 M LiTFSI DOL/

DME (1:1 v/v) by spatial constraint of polysulfides near the sulfur composite cathode. On the contrary, micropores improve the stability of the Li–sulfur battery by hindering the carbon structure disintegration during cycling.

Experimental

The cathodes for sulfur-free electrochemical tests were prepared as follows: The carbon (Fluka—Activated Charcoal (C_{Fluka}), Penta—Activated Carbon (C_{Penta}), or TOB New Energy—TOB-HPC (C_{TOB})) was mixed in an agate mortar with the conductive carbon black C65 (Timcal) and 2% aqueous solution of carboxymethylcellulose (Sigma) added and mortared again. The final mass ratio of the carbon to C65 and carboxymethylcellulose was 5:4:1. Subsequently, the viscous paste was created by adding deionized water into the mixture and deposited on the aluminum mesh by dip coating. The final Al mesh was dried at 50 °C under a vacuum overnight and the electrodes were stored under an Ar atmosphere in a glove box.

The cathodes for Li–S coin cells were prepared by a procedure reported previously by Zlamalova et al. [44] Briefly, carbon C_{Fluka}, C_{Penta}, or C_{TOB} was mixed with sulfur (Sigma-Aldrich) in a mass ratio of 1:4 and mortared in an agate mortar for 20 min. Subsequently, the mixture was heated at 155 °C for 15 h under an Ar atmosphere in a Teflon container and mortared again. The conductive carbon black C65 (Timcal) and 2% aqueous solution of carboxymethyl-cellulose (Sigma) were added and mortared. The final mass ratio of the carbon/sulfur composite to C65 and carboxy-methylcellulose was 7:2:1. The as-prepared cathode material contained 56 wt% of sulfur. The concentration of sulfur was verified by X-ray fluorescence spectroscopy (XRF) analysis reported previously [45]. Subsequently, the viscous paste was created by adding deionized water to the mixture. The resulting slurry was stirred at 400 RPM overnight and deposited on aluminum foil by doctor-blading. The coated Al foil was dried at 50 °C under a vacuum overnight and cut into disc electrodes of 15 mm in diameter. The areal sulfur loading was adjusted to 0.5–0.6 mg/cm^2. The electrodes were stored under an Ar atmosphere in a glove box. The electrodes were assembled in 2032 coin-type test cells with Li-foil anode (14 mm in diameter), glass microfiber separator (Whatman), and 20 mm^3 of electrolyte.

The electrolyte for sulfur-free electrochemical tests and Li–S coin cells tests was identical. It consisted of 1.0 M lithium bis-(trifluoromethanesulfonyl) imide (LiTFSI, Aldrich) dissolved in a mixture of 1,3-dioxolane (DOL) and 1,2-dimethoxyethane (DME) (1:1 by volume) with 1.0 wt% $LiNO_3$ (Aldrich) as an electrolyte-additive. LiTFSI was dried in a vacuum at 130 °C overnight, $LiNO_3$ at 50 °C in a vacuum overnight, and the mixture of organic solvents was dried over a molecular sieve 4 Å (Aldrich). Electrolytes, solvents, and redox-active molecules were of standard quality (p.a. or electrochemical grade) purchased from Aldrich or Merck.

Raman spectra were measured on the MicroRaman system (LabRAM HR spectrometer, Horiba Jobin–Yvon) with an Olympus BX microscope. The spectra were excited by a He–Ne laser (633 nm). The Raman spectrometer was calibrated using the F_{1g} line of Si at 520.5 cm^{-1}. The intensities of the D and G-band were determined by fitting the spectra with a Lorentzian function. The adsorption isotherms of nitrogen were measured with ASAP 2020 apparatus (Micromeritics) at 77 K. Before the adsorption measurement, each sample was degassed at 300 °C for at least 3 h under a pressure less than 0.7 Pa. After the free space was determined at 77 K with helium the samples were evacuated for an additional 3 h at 250 °C. The surface area was determined by the BET (Brunauer, Emmett, Teller) equation. The BET surface areas of carbonaceous materials containing micropores in the structure have been calculated using Rouquerol's criteria [42]. The surface area out of micropores was determined by *t*-plot analysis (thickness equation—Carbon Black STSA). Sulfur-free electrochemical measurements were carried out in a one-compartment cell using Autolab 302N apparatus (Metrohm) controlled by Nova software in the potential window from 2 to 3 V vs Li/Li$^+$. The reference and counter electrodes were from Li metal; hence, all potentials were quoted against the reference electrode in this medium. The electrochemical measurements were carried out under an argon atmosphere in a glove box. The Li–S coin cell tests were carried out with Autolab 302N apparatus (Metrohm) controlled by Nova and Nova Battery SW in 2032 coin-type test cells at a potential window of 1.7–2.9 V vs. Li$^+$/Li. Galvanostatic chronopotentiometry was measured in the 2032 coin-type test cells by the Neware Battery Testing System controlled by BTS 7.6 SW.

Data availability Data will be available from the corresponding author upon request.

need to obtain permission directly from the copyright holder. To view a copy of this licence, visit http://creativecommons.org/licenses/by/4.0/.

References

1. Ould Ely T, Kamzabek D, Chakraborty D, Doherty MF (2018) ACS Appl Energy Mater 1:1783
2. Eftekhari A, Kim DW (2017) J Mater Chem A 5:17734
3. Jiang JC, Fan QN, Liu HK, Chou SL, Konstantinov K, Wang JZ (2021) ACS Appl Mater Inter 13:28405
4. Cleaver T, Kovacik P, Marinescu M, Zhang T, Offer G (2018) J Electrochem Soc 165:A6029
5. Dorfler S, Althues H, Hartel P, Abendroth T, Schumm B, Kaskel S (2020) Joule 4:539
6. Yin YX, Xin S, Guo YG, Wan LJ (2013) Angew Chem Int Ed 52:13186
7. Mi K, Jiang Y, Feng JK, Qian YT, Xiong SL (2016) Adv Funct Mater 26:1571
8. Lin DC, Liu YY, Cui Y (2017) Nat Nanotechnol 12:194
9. Zhu W, Paolella A, Kim CS, Liu D, Feng Z, Gagnon C, Trottier J, Vijh A, Guerfi A, Mauger A, Julien CM, Armandd M, Zaghib K (2017) Sustain Energy Fuels 1:737
10. Peng HJ, Huang JQ, Cheng XB, Zhang Q (2017) Adv Energy Mater 7:1700260
11. Wang XZ, Zhang S, Zhang HY, Gao S, Han SJ, Xu QY, Xu JJ, Lu W, Wu XD, Chen LW (2019) ACS Sustain Chem Eng 7:17491
12. Luo C, Niu SZ, Zhou GM, Lv W, Li BH, Kang FY, Yang QH (2016) Chem Commun 52:12143
13. Jeong YC, Lee K, Kim T, Kim JH, Park J, Cho YS, Yang SJ, Park CR (2016) J Mater Chem A 4:819
14. Ding YL, Kopold P, Hahn K, van Aken PA, Maier J, Yu Y (2016) Adv Funct Mater 26:1112
15. Zhu X, Ye JW, Lu YF, Jia XL (2019) ACS Sustain Chem Eng 7:11241
16. Nguyen QH, Luu VT, Lim SN, Lee YW, Cho YY, Jun YS, Seo MH, Ahn W (2021) ACS Appl Mater Inter 13:28036
17. Nitze F, Fossum K, Xiong SZ, Matic A, Palmqvist AEC (2016) J Power Sources 317:112
18. Hencz L, Wu ZZ, Zheng MT, Bat-Erdene M, Qian SS, Su Z, Gu XX, Liu XH, Zhang SQ, Chen H (2022) ACS Appl Energy Mater 5:4991
19. Zou YW, Guo DY, Yang B, Zhou L, Lin PR, Wang JY, Chen XA, Wang S (2021) ACS Appl Mater Inter 13:50093
20. Li X, Li XF, Banis MN, Wang BQ, Lushington A, Cui XY, Li RY, Sham TK, Sun XL (2014) J Mater Chem A 2:12866
21. Rouquerol F, Rouquerol J, Sing KSW, Llewellyn P, Maurin G (2014) Adsorption by powders and porous solids principles, methodology and applications. Academic Press, Oxford
22. Lippens BC, Linsen BG, Deboer JH (1964) J Catal 3:32
23. Deboer JH, Linsen BG, Osinga TJ (1965) J Catal 4:643
24. Lowell S, Shields JE, Thomas MA, Thommes M (2004) Characterization of porous solids and powders: surface area, pore size and density. Kluwer Academic Publishers, Dordrecht
25. Wang SW, Vallejos-Burgos F, Furuse A, Yoshikawa Y, Tanaka H, Kaneko K (2021) Carbon 175:77
26. Setoyama N, Suzuki T, Kaneko K (1998) Carbon 36:1459
27. Kaneko K, Ishii C, Kanoh H, Hanzawa Y, Setoyama N, Suzuki T (1998) Adv Colloid Interface Sci 76–77:295
28. Kaneko K, Ishii C, Ruike M, Kuwabara H (1992) Carbon 30:1075
29. Borchardt L, Oschatz M, Kaskel S (2016) Chem Eur J 22:7324
30. Zhang SS (2013) J Power Sources 231:153
31. Kensy C, Schwotzer F, Dorfler S, Althues H, Kaskel S (2021) Batteries Supercaps 4:823
32. Yu CH, Yen YJ, Chung SH (2021) Nanomaterials 11:1518
33. Kensy C, Leistenschneider D, Wang S, Tanaka H, Dorfler S, Kaneko K, Kaskel S (2021) Batteries Supercaps 4:612
34. Choi YS, Park GO, Kim KH, Kwon Y, Huh J, Kim JM (2021) Chem Commun 57:10500
35. Tonoya T, Ando H, Takeichi N, Senoh H, Kojima T, Hinago H, Matsui Y, Ishikawa M (2023) J Phys Chem C 127:10038
36. Ferrari AC, Robertson J (2000) Phys Rev B 61:14095
37. Ferrari AC (2007) Solid State Commun 143:47
38. Tuinstra F, Koenig JL (1970) J Chem Phys 53:1126
39. Cancado LG, Jorio A, Ferreira EHM, Stavale F, Achete CA, Capaz RB, Moutinho MVO, Lombardo A, Kulmala TS, Ferrari AC (2011) Nano Lett 11:3190
40. Smith MW, Dallmeyer I, Johnson TJ, Brauer CS, McEwen JS, Espinal JF, Garcia-Perez M (2016) Carbon 100:678
41. Kaneko K, Ishii C (1992) Colloid Surf 67:203
42. Rouquerol J, Llewellyn P, Rouquerol F (2006) Stud Surf Sci Catal 160:49
43. Li Z, Jiang Y, Yuan LX, Yi ZQ, Wu C, Liu Y, Strasser P, Huang YH (2014) ACS Nano 8:9295
44. Zlamalova M, Pitna Laskova B, Vinarcikova M, Zukalova M, Kavan L (2022) J Solid State Electrochem 26:639
45. Zukalová M, Vinarčíková M, Pitňa Lásková B, Kavan L (2023) Mater Chem Phys 296:127246